

# Assessment of the Feasibility of Using a Synchronous Homopolar Motor Instead of an Induction Motor in a Traction Drive With a Wide Constant Power Speed Range

VLADIMIR PRAKHT <sup>1</sup>, VLADIMIR DMITRIEVSKII <sup>2</sup>, VADIM KAZAKBAEV <sup>1</sup>, EDUARD VALEEV,  
ALEKSEY PARAMONOV, AND ALECKSEY ANUCHIN <sup>1</sup> (Senior Member, IEEE)

<sup>1</sup>Electrical Engineering Department, Ural Federal University, 620002 Yekaterinburg, Russia  
<sup>2</sup>Department of Electric Drives, Moscow Power Engineering Institute, 111250 Moscow, Russia

CORRESPONDING AUTHOR: ALECKSEY ANUCHIN (e-mail: anuchinas@mpei.ru).

This work was supported by the Ministry of Science and Higher Education of the Russian Federation under Project FSWF-2023-0017.

**ABSTRACT** Synchronous homopolar machines (SHMs) have established their merit in various applications, including pulse heating generators and automotive generators. They offer such advantages as a simple and dependable rotor design devoid of windings and permanent magnets, and a reliable field winding consisting of a small number of concentrated coils on the stator. This makes SHMs promising as traction motors for off-highway vehicles, such as mining dump trucks. Mining dump trucks confront the challenges of transporting hefty loads on dirt roads at speeds up to 60 km/h and conquering steep inclines. Although conventional induction motors (IMs) are widely used in these trucks, they suffer from rotor overheating, vulnerability to broken rotor bar faults, and substantial low-frequency current oscillations when braking on a slope. These problems stimulate the search for alternatives. This article conducts a theoretical analysis comparing optimized designs of IM and SHM for driving a mining dump truck with a payload of 90 tons. The comparison encompasses critical parameters such as efficiency, losses, torque ripple, required inverter power, dimensions, weight, active material cost, and inverter reliability. The study employs the downhill simplex method for optimization and the finite element method. The study shows that the benefits of SHM include reduced active material costs and improved motor and inverter reliability.

**INDEX TERMS** Constant power speed operation range, haul truck, synchronous machines with DC excitation, synchronous homopolar motor, Nelder-Mead optimization algorithm, optimum design, induction machines, vehicle traction drive systems, wound field synchronous motors.

## I. INTRODUCTION

### A. ADVANTAGES OF SYNCHRONOUS HOMOPOLAR MOTORS WITHOUT RARE EARTH MAGNETS

Currently, electric vehicles can use different types of motors. Permanent magnet synchronous motors (PMSM) are compact but expensive and have uncontrolled magnet flux [1]. This increases the risk of fire in emergency situations and makes it difficult to obtain a wide constant power speed range (CPSR). In addition, rare earth magnets have low temperature resistance.

This increases the risk of fire in emergency situations and makes it difficult to obtain a wide constant power speed range (CPSR). In addition, rare earth magnets have a low temperature resistance. Due to the shortcomings, the problem of developing traction motors without rare-earth magnets is urgent [2], [3], [4], [5], [6], [7].

Widely used induction motors (IM), used for example in Audi etron S and Tesla Model S [8], [9], [10], [11], [12], [13], [14], in addition to their bulkiness, also have an increased risk of failure of the welded rotor cage and bearings due to high

rotor overheating. In addition, the reliability of the traction inverter when using an IM may be reduced due to large temperature pulsations during braking mode at zero-speed [15], [16], [17], [18], [19], [20], [21], [22], [23], [24], [25], [26], [27], [28].

Wound field synchronous motors (WFSMs), used for example in BMW iX3, Renault Zoe, Renault Fluence, and Renault Megane E TECH [29], [30], [31], [32], [33], although potentially well suited for providing a wide CPSR in a traction drive, are limited in their reliability by the sliding contact for feeding the field winding on the rotor [34], [35]. WFSMs with a brushless exciter are also known, but increasing complexity and cost limit their use [36].

An alternative would be to use synchronous homopolar motors (SHM) without permanent magnets and with an excitation winding on the stator.

In addition to eliminating sliding contacts, SHMs offer advantages over WFSMs, including higher reliability, absence of electrical losses in the rotor, simplified rotor cooling systems, and a more straightforward and dependable design of the excitation winding, comprising ring-shaped coils mounted on the stator.

SHMs, like all stator-mounted PM and wound field machines, have such an advantage as a rugged and simple rotor and are suitable for high-speed or high-torque applications [45]. Like other PM machines, stator-mounted PM machines do not allow controlling excitation MMF, which decreases possibilities of extending CPSR. SHM, on the other hand, belongs to machines with a stator excitation winding, which allows for a wider CPSR.

SHMs are typically used as highly reliable generators [37], [38], [39], [40], but their use as traction motors has also been proposed [41], [42], [43], [44].

## **B. DESIGN OPTIMIZATION OF INDUCTION MOTORS FOR ELECTRIC VEHICLES**

In the context of developing electric motors for off-highway cargo vehicles, this article further examines and compares the performance of a synchronous homopolar machine (SHM) and an induction machine (IM). Specifically, the comparison focuses on their suitability for a hybrid mining dump truck, operating within a speed range of 400 to 4000 rpm, while maintaining a constant mechanical power output of 370 kW (corresponding to a CPSR of 10:1).

Generally, motors for highway electric vehicle need a CPSR of no more than 4:1 [46]. However, off-road and off-highway electric vehicles require a wider CPSR [43]. Typically, the expansion of a CPSR is achieved by increasing the power, maximum current, and cost of the solid-state inverter [47]. However, as shown in this article, optimizing the motor to minimize the current at two operating points (at base speed and at maximum speed) can help avoid the excessive increase in power and cost of the inverter when a wide CPSR is required.

The article includes a cost analysis that compares the expenses associated with the active materials of the electrical

motors and the semiconductor inverter power modules for both SHM and IM. In addition, it is shown that the use of the SHM improves the reliability and prolongs the service life of the traction semiconductor inverter by eliminating temperature ripple of the power switches in the electric braking mode when stopped on a slope, which is often used for mining dump trucks [48].

For instance, in [49], a comprehensive comparison of performance among various traction motors, including interior permanent magnet synchronous motors (IPMSM), surface permanent magnet synchronous motors (SPMSM), and IM, is undertaken within the context of a CPSR of 3:1. The assessment involves scrutinizing the attributes of these motors, with the calculation of IM characteristics relying on magnetostatic FEA coupled with an analytical estimation of rotor currents. Notably, the analysis refrains from employing computer-aided optimization of motor characteristics before conducting the comparative study. The outcomes of this investigation underscore the advantageous positions of IPMSMs and IMs over SPMSMs within a broader CPSR range. It is pertinent to note that despite this advantage, IMs are identified to exhibit heightened losses in contrast to IPMSMs.

In [50], a parallel examination delves into the performance disparities of high-speed IPMSM, Switched Reluctance Motor (SRM), and IM in a traction application characterized by a CPSR of 5:1. In this study, the calculation of the characteristics of the IM is performed using FEA, carried out in the time domain, taking into account the spatial harmonics of the magnetic field. The insights garnered from this study highlight the efficacy of IPMSMs in compact dimensions and the potency of SRMs in contexts demanding robust rotor strength. Meanwhile, IMs offer distinct advantages, including immunity to irreversible demagnetization risks, mitigation of magnet losses, and attenuation of ventilation losses. However, the notable drawback associated with IMs pertains to their significantly higher total power losses relative to IPMSMs.

Paper [50] compares the performance of an induction motor and a wound field synchronous motor (WFSM) in a drive with a CPSR of 10:1. The characteristics of the compared motors are pre-optimized using the Nelder-Mead method. The performance of WFSM is calculated from magnetostatic FEA, while for IM the time domain finite element method is used. It is shown that WFSM, compared to IM, provides reduced losses and increased reliability. It is also shown that in a drive with a CPSR of 10:1, an induction drive with a rated power of 370 kW requires an inverter with a power rating of 1689 kVA, while a WFSM drive requires only 1169 kVA.

## **C. THE PROBLEM AND AIM OF THE STUDY**

Based on the above, it can be concluded that the scientific novelty of this study lies in comparing the characteristics of the SHM and IM, including efficiency, torque ripple, required power and temperature ripple in the solid-state inverter, in a traction application with a wide CPSR of 10:1, which has not been previously presented in the literature. The above characteristics of the IM are compared with those of the SHM

**TABLE I** Technical Specifications of the Traction Motor

Parameter	Value
Rated power, kW	370
Peak torque, N·m	8833
Rated speed, rpm	400
Maximum speed, rpm	4000
Phase number	9
DC-link voltage, V	1000

obtained in a previous study [43]. Both motors underwent design optimization using similar approaches, including the Nelder-Mead method and two-dimensional FEA.

Some differences in the methodology for evaluating the characteristics and optimization of the IM, compared to the SHM, are associated only with the features of the IM. The SHM has no currents in the rotor. At the same time, when calculating IM performance, it is necessary to calculate currents that are induced in the short-circuited rotor winding by the alternating magnetic field of the air gap. This requires FEA of the IM in the time domain, and, as a result, significantly increases the calculation time, while the magnetostatic FEA for several rotor positions is sufficient for the SHM.

This article continues the comparative studies of various types of traction motor with a very wide CPSR of 10:1 in off-highway cargo vehicles presented by the authors in [7], [44], [51]. In [7], the SHM was compared with a PMSM. In [44], the SHM was compared with a WFSM. In [51] the WFSM was compared with the IM. However, the comparison of the SHM with the IM in this specific application has not yet been carried out in the literature. This comparison is especially important from a practical point of view because IMs are used in most mining dump trucks [8], [19], [20].

**II. DESIGN CHARACTERISTICS OF THE EVALUATED MOTORS**

Table I shows the required traction motor characteristics for this application, which both IM and SHM must satisfy.

The structure of the IM magnetic core is homogeneous along the axis of rotation, so it is sufficient to consider the two-dimensional geometry in its mathematical model (Fig. 1(a)). The SHM consists of three pairs of stator and rotor laminated stacks connected by axial elements that conduct the excitation magnetic flux. Therefore, to model the magnetic circuit the SHM, it is necessary both to consider the two-dimensional geometry of a pair of stator and rotor stacks (Fig. 1(b)), and to consider the design of the axial elements: the stator housing and the rotor hub (Fig. 1(c)). Fig. 1 illustrates the motor phases denoted by capital letters A to I, representing their sequential order. The negative sign in Fig. 1 signifies the reversed current direction within a winding layer.

Both motors under consideration feature a 9-phase winding configuration. From the point of view of the simplicity of the electric drive, it is desirable to minimize the number of motor phases to three. However, in the considered case, the armature winding consists of three three-phase subwindings

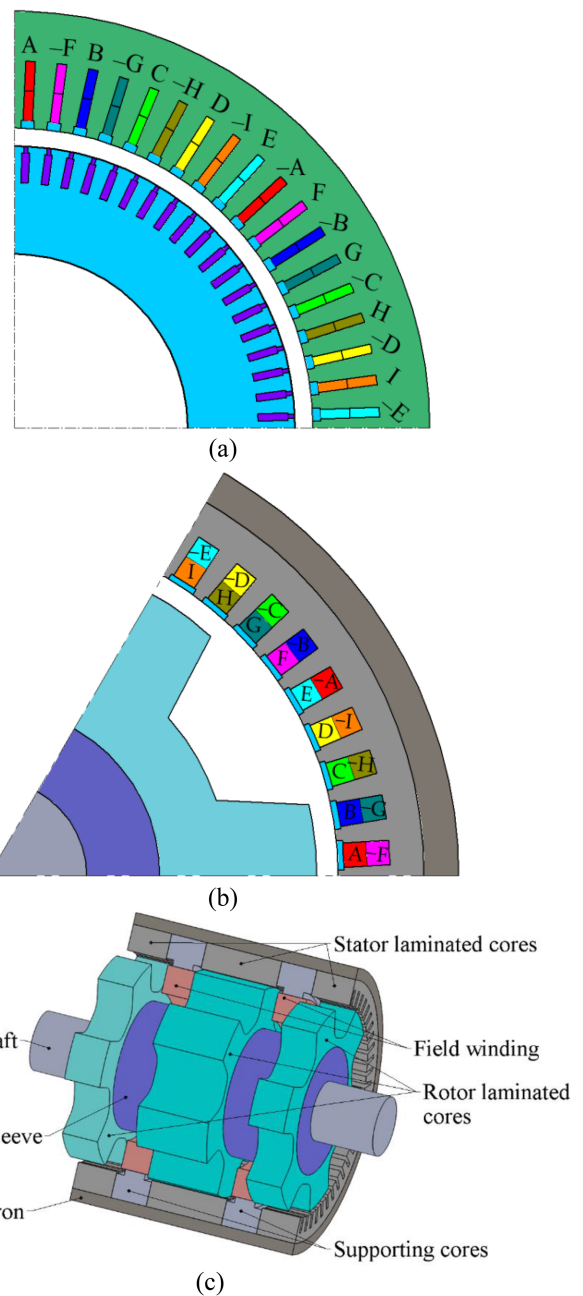


**FIGURE 1.** Representation of the motor design: (a) Induction motor (IM) 2 pole area; (b) Synchronous homopolar motor (SHM) winding layout on 2 pole area; (c) SHM 3D structure.

forming a nine-phase winding, each of which has its separate neutral point. This is done to reduce the current in each phase to simplify the design of the traction inverter [41]. In addition, the fault tolerance of the drive is increased: in the event of a phase failure, the drive can continue to operate without a very large reduction in load capacity. The phase shift between adjacent phases is  $360^\circ/9 = 40$  electrical degrees.

The SHM stator has 12 poles, 54 slots and the number of slots per pole and per phase  $q = 54/(12 \cdot 9) = 0.5$ . The IM stator has 8 poles, 75 slots and the number of slots per pole and per

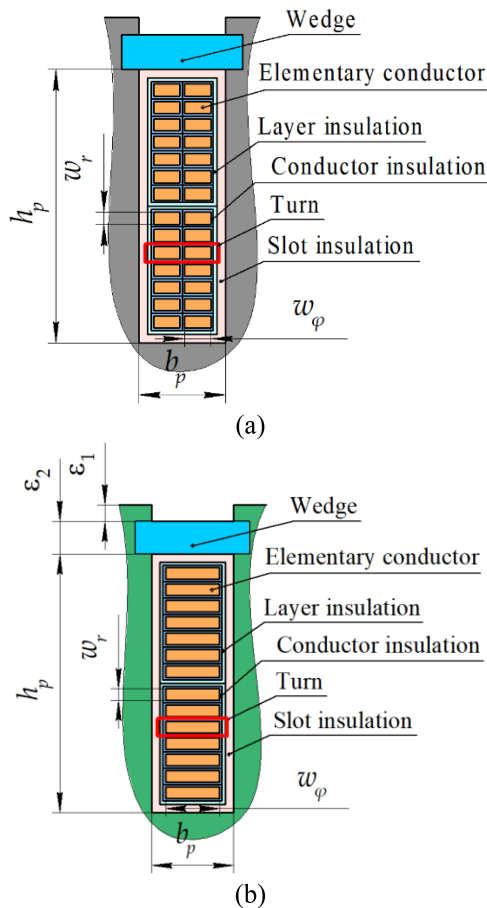


FIGURE 2. Open type stator slot sketch. (a) SHM; (b) IM.

phase  $q = 72/(8 \cdot 9) = 1$ . The SHM uses a two-layer winding (Fig. 2(a)). The IM uses a single layer winding (Fig. 2(b)).

The magnetic cores of both the stator and rotor are constructed from M270-35A steel, each with a 0.35 mm thickness. The IM rotor comprises 76 slots, within which rectangular-shaped squirrel cage bars are positioned. These rotor bars are short-circuited by end rings, featuring openings at the bar ends. Following the welding of the rings to the bars, these openings are sealed, resulting in plates that can be treated as solid disks.

This study is about motors utilizing a nine-phase inverter, as illustrated in Fig. 3. This inverter consists of three distinct three-phase modules, with each module providing power to three motor phases. The maximum amplitude of the line-to-line voltage is capped at 1000 V, aligning with the limits of the DC link voltage. Discontinuous space-vector modulation is employed for each of these three-phase modules [57]. There are several advantages to using a nine-phase inverter. It diminishes the current ratings required for individual power modules, thereby boosting reliability in the event of module malfunction [28], [58]. The nine-phase inverter circuit used includes 3 separate three-phase inverters. This allows the use of more common inverter power modules for the power and voltage ratings in question. In addition, if

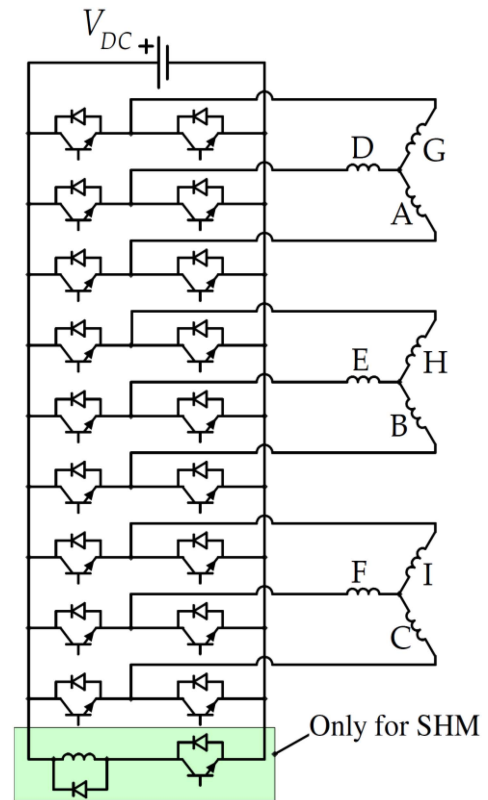


FIGURE 3. Design layout of the nine-phase inverter to supply the motor.

one of the three-phase inverters fails, the other two continue to work and the drive remains operational.

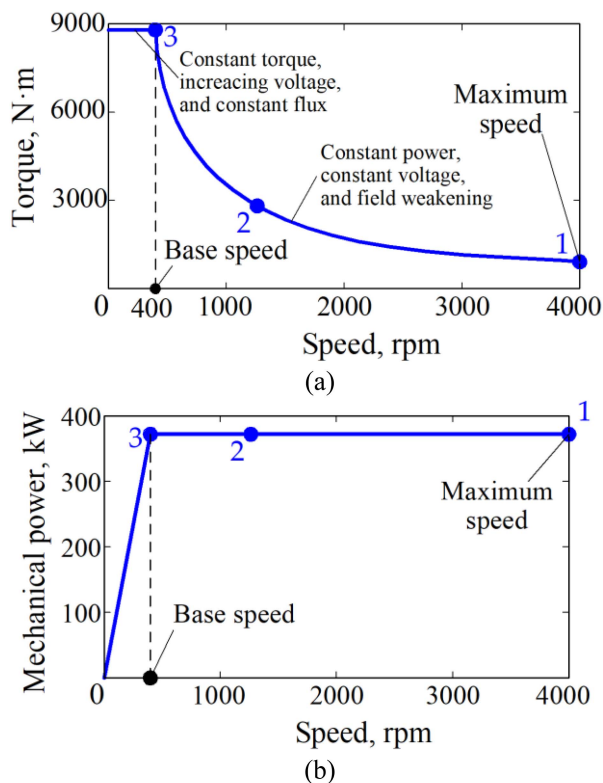
Additionally, the motor's adoption of a nine-phase winding enhances both winding factor and the spectral composition of the magnetomotive force, further contributing to improved motor performance.

As is known, in the spectrum of the MMF of the armature winding in the air gap of a 3-phase machine there are harmonics  $\nu = 3n+1$  where  $n \in \mathbb{Z}$  [59]. It is because of the symmetry of shifting the windings slots by third of the MMF period in the gap with shifting the current phases by  $2\pi/3$ . There is higher symmetry in the 9-phase winding: shifting the winding slots by ninth of the field period with shifting the current phases by  $2\pi/9$ . Therefore, there are only harmonics  $\nu = 9n+1$  in the MMF.

So, the nine-phase winding eliminates some of these parasitic harmonics. In MMF spectrum of the SHM with the number of phases 9 and 9 stator teeth the MMF period, there are no harmonics from  $-7$ th to 9th. In a three-phase winding with the same 9 stator teeth per period in this interval there are MMF harmonics  $-5$ th,  $-2$ nd and 4th, 7th. In the IM with an even number of stator slots per period (18 slots), additional symmetry of shifting the winding by a pole pitch and changing the current signs suppresses even harmonics. So, in the 9-phase IM, there are no  $-5$ th and 7th harmonics, while the  $-2$ th and 4th harmonics are absent in both 3- and 9-phase cases.

**TABLE II** Winding Coefficients of Various Designs

Motor type	3-phase SHM	9-phase SHM	3-phase IM	9-phase IM
Number of stator slots per period	9	9	18	18
Winding pitch in tooth pitches	4	4	9	9
Winding coefficient	0.947	0.985	0.987	1

**FIGURE 4.** Characteristics of the traction electric drive under consideration: (a) Torque-Speed curve; (b) Output power-speed curve. Operating points 1, 2, and 3 indicated as per Table IV.

To suppress parasitic harmonics in the MMF and EMF spectrum, in addition to increasing the number of phases, shortening the winding pitch can also be used. But such suppression does not mean elimination completely. In addition, this technique reduces the winding coefficient.”

The fundamental harmonic winding coefficients are given in Table II.

Detailed information regarding the parameters, objectives, and optimization results of the synchronous homopolar machine (SHM) can be found in [43]. Hence, this article exclusively presents the results of the induction machine (IM) optimization. The compared motors must satisfy the traction characteristic requirements of the BELAZ 75570 mining truck drive, as depicted in Fig. 4. The drive is required to deliver a mechanical power output of 370 kW within a speed range of 400 rpm to 4000 rpm (10:1).

CPSR (also known as “constant power region”) is defined by the ratio of maximum to rated speed (also known as “base speed”). The range from zero to base speed is determined by constant torque, constant flux and increasing voltage with increasing speed. The constant power region is determined by constant power, decreasing flux with increasing speed and constant voltage (see Fig. 4(a)) [46].

In the proposed synchronous homopolar machine (SHM), the main part of the torque is created due to the interaction of the armature current with the magnetic flux of the field winding. That is, the SHM belongs to the class of electrically excited synchronous machines [60]. Unlike conventional reluctance machines, the controllability of the magnetic flux of the SHM field winding extends the capability of field weakening and obtaining a wider constant power speed range (CPSR) [61], which is in demand, for example, in traction applications.

In the case of SHM, field weakening is achieved by adjusting the  $d$ -axis component of the armature current as well as the field current. In the case of IM, field weakening is obtained inherently with increasing the slip due to the demagnetizing effect of the squirrel cage according to Lenz’s law.

In terms of fault-tolerant performance, both the IM and SHM have similar capabilities. Due to the large number of phases, if one or two phases fail, the motors can remain partially operational if the inverter algorithms allow this. Also, the risk of failure of the SHM drive will be less due to the absence of a squirrel cage on the rotor, as well as due to the absence of temperature pulsations in the inverter modules when parked on an incline, as explained in Section VII.

### III. APPROACH TO MATHEMATICAL MODELING OF THE INDUCTION MOTOR IN STEADY STATE

This section presents our original computationally efficient technique for designing an induction motor using time domain FEA.

In this study characteristics of the SHM and IM are calculated for given sinusoidal stator phase currents. In the SHM, there are no currents in the rotor, and the distribution of stator currents is known in advance. Therefore, the calculation of characteristics of the SHM is possible based on a sequence of magnetostatic boundary value problems for various positions of the rotor.

In the context of IMs, a crucial aspect involves the computation of the current density distribution within the rotor bars. Various methodologies exist for modeling IMs in steady state [62], [63] but to comprehensively address effects like core saturation over time and minor harmonics, a time domain finite element modelling is indispensable.

The time-domain two-dimensional FEA of IMs is typically conducted, assuming sinusoidal phase currents and a plane-parallel magnetic field. This field is defined by a vector magnetic potential, primarily featuring the normal component  $A_z$ . The magnetic field refer to (1)-(3) are employed to characterize this phenomenon [62]. The constituent components

of the magnetic flux density adopt the following format:

$$B_x = \frac{\partial A_z}{\partial y}; B_y = -\frac{\partial A_z}{\partial x}. \quad (1)$$

The relationship of the magnetic field strength  $H$  with respect to the flux density  $B$  is determined using constitutive equations. The quantities  $B$ ,  $H$ , and  $A_z$  are influenced by the current density perpendicular to the cross-sectional plane, following Ampère's law:

$$\frac{\partial H_y}{\partial x} - \frac{\partial H_x}{\partial y} = J_z. \quad (2)$$

The current density in phase windings and their associated flux linkage are characterized as:

$$J_z = \sum_i I_i \Xi_i; \quad \Phi_i = L \iint A_z \Xi_i dS, \quad (3)$$

where  $L$  is the length of the stator lamination;  $\Xi_i$  is the current density, when 1 A current flows through the  $i$ -th phase while other phases remain inactive.

The instantaneous phase voltage is determined through the instantaneous flux linkage, as suggested by formula (4):

$$U_i = \frac{d\Phi_i}{dt} + RI_i, \quad (4)$$

where  $R$  is the resistance of one motor phase.

Windings employing compact rectangular conductors and featuring a low turn count per coil experience both DC losses and notable eddy current losses [64]. The eddy current loss density in the winding described in (5).

$$p_{eddy} = \frac{\sigma_{Cu} k_z}{12} \left[ w_\phi^2 \left( \frac{\partial B_r}{\partial t} \right)^2 + w_r^2 \left( \frac{\partial B_\phi}{\partial t} \right)^2 \right], \quad (5)$$

where  $\sigma_{Cu}$  is the electrical conductivity of copper;  $w_\phi$  and  $w_r$  are the wire section's width and height;  $k_z$  is the slot filling factor;  $B_r$  and  $B_\phi$  are the flux density's radial and tangential components, respectively.

The current density in the  $i$ -th rod of the rotor squirrel cage described in (6):

$$J_z = -\sigma_{squirrel} \left( \frac{dA_z}{dt} + \frac{\phi_i}{L} \right), \quad (6)$$

where  $d/dt$  is the substantial time derivative;  $\phi_i$  is the potential difference at the ends of the rotor bars.

Equation (7) defines the potential difference.

$$2\phi_i - \phi_{i-1} - \phi_{i+1} = 2r_{rot} I_i^{squirrel}, \quad (7)$$

where  $r_{rot}$  corresponds to the resistance of a section of the squirrel cage over one rotor tooth pitch. Equation (8) represents the current flowing through the  $i$ -th rotor rod. Coefficient 2 on the right side of the equation takes into account the restriction of the rod by two end rings.

$$I_i^{squirrel} = \int_{i-th \text{ rod}} J_z dS, \quad (8)$$

In a section with a length equivalent to one pitch of the rotor poles, the arc length is  $2\pi r/N_{rot}$ , where  $N_{rot}$  denotes the number of rotor rods and  $r$  is the distance from the rotation axis. Assuming a constant potential  $\varphi$  across the cross sections of rings that demarcate one rotor tooth pitch, and a current density inversely proportional to the arc's length, the squirrel cage resistance per rotor pitch can be computed as  $r_{rot} = 2\pi / (N_{rot} \cdot h \cdot \sigma_{squirrel} \cdot \ln[R_{ring1}/R_{ring2}])$ , where  $h$  is the ring thickness,  $\sigma_{squirrel}$  is the squirrel cage material's conductivity, and  $R_{ring1}$  and  $R_{ring2}$  denote the external and internal radii of the rings.

To simplify the calculation of the substantial derivative, in fact to replace it with partial one, and to use the same geometry for all rotor positions, the calculation area is split into the rotor and stator parts by the arc in the middle of airgap. The rotor rotation is taken into account by means of the time boundary condition joining these parts.

Employing a time-domain 2D model for induction motor analysis yields high accuracy, albeit demanding substantial computational resources due to prolonged transients [62], [63]. This is a serious obstacle to computer-aided optimization of an IM design. This study shows an approach that speeds up the transient by reducing the conductivity of the squirrel cage material.

To implement this at each moment of time, the specific conductivity of the squirrel cage material decreases by the same factor as the frequency in the rotor squirrel cage increases while the rotor rotational speed is assumed to be constant. This coefficient has a large value at the beginning and decreases with increasing simulation time, reaching a value of 1 when a steady-state condition of the IM is reached. In the steady state, the simulation is already carried out as usual.

Such a simultaneous change in the frequency of feeding and the specific conductivity of the squirrel cage has the following features: 1) It does not change the torque at the same current in the rotor; 2) It does not change the skin effect depth of the squirrel cage material.

The accelerated transient process is described in (9):

$$\begin{aligned} \sigma_{squirrel} &= \frac{\sigma_{squirrel0}}{m}; \\ \omega &= p\Omega \left( 1 + \frac{sm}{1-s} \right); \\ \varphi &= \int_0^t \omega dt; \\ m &= 1 + m_0(1 - t/t_0)^\gamma, \quad t < t_0; \\ m &= 1, \quad t \geq t_0, \end{aligned} \quad (9)$$

where  $\sigma_{squirrel0}$  and  $\sigma_{squirrel}$  are the real and fictitious used in the calculation of the electrical conductivity of the squirrel cage material;  $p$  is the pole number;  $\Omega$  is the mechanical rotor angular frequency;  $\omega$  is the electric angular frequency taken during the calculation;  $\varphi$  is the electrical current angle; parameters  $m_0$  and  $\gamma$  define the relationship  $m(t)$ ;  $t_0$  is the time

from the beginning of the calculation of the transient process to the establishment of a steady state.

The spatial discretization of the model is performed using triangular Lagrangian elements of the 2nd order. The time discretization of the model employs a constant step using the second-order inverse differentiation formula (BDF). Note that very large changes in the current phase at one step are allowed at the beginning of the calculation. The fact is that BDF intended for solving rigid systems ensures the stability of the solver, including in the high-frequency region of the spectrum. With increasing argument  $t$ , parameter  $m$  exhibits a decline, enhancing the precision of BDF derivative approximations. Employing a mathematical model typically entails computing particular points with designated speed, torque, and power. This research introduces slip as an additional calculation input, selecting the current to achieve the desired power at a given speed. To implement this, additional differential (10) is concurrently solved:

$$\frac{dI}{dt} = \alpha (P_{20} - P_2) \tag{10}$$

where  $P_{20}$  and  $P_2$  are the set and instantaneous values of the mechanical power;  $\alpha$  is the constant that determines the rate of termination of the rotor current transient;  $I$  is the current amplitude.

**IV. ADVANTAGE OF THE NELDER-MEAD METHOD IN OPTIMIZING TRACTION ELECTRIC MACHINES**

The optimal design of a traction motor intended to operate in a wide CPSR makes it necessary to take into account several operating points, but this entails an increase in computational burden by several times [52].

Utilizing the simplex Nelder-Mead method offers substantial optimization time reduction in comparison to population-based methods like genetic algorithms and particle swarm algorithms commonly employed for electrical machine optimization [52], [53], [54], [55], [56]. This efficiency gain facilitates the expansion of the optimized parameter set and the application of intricate optimization criteria, necessitating computations across multiple machine load points [43]. This advantage proves especially valuable in optimizing traction machines with a broad CPSR.

As can be seen from Table III, the Nelder-Mead (NM) method requires several times fewer function calls to complete the optimization than popular population methods for optimizing electrical machines, such as particle swarm optimization (PSO), genetic algorithms (GA), differential evolution (DE), etc., which means, ceteris paribus, and less computing time.

Thus, in [52], the characteristics of the PMSM in the NEDC motion cycle were optimized using DE. In this case, to reduce the calculation time, the NEDC cycle is replaced by an equivalent cycle of 4 operating points. This approach requires 26 DE iterations with a population size of 36 and 3744 motor calculations to perform the optimization search. At the same time, due to the large computational burden, the

**TABLE III Comparison of Reported Computational Burden When Optimizing a Motor Design**

Motor type	Output power, kW	CPSR	Optimization algorithm	Operating points, $n$
PMSM	75	2:1	PSO	1
SynRM	1.2	-	GA	1
PMSM	85	2.7:1	DE	1
SynRM	2	-	DE	1
PMSM	11.8	2.55:1	DE	4
SHM	370	10:1	NM	3

Motor type	Function calls, $k$	Population size, $j$	Number of machine calculations, $n \cdot k \cdot j$	Reference
PMSM	100	100	10000	[55]
SynRM	250	50	12500	[56]
PMSM	100	30	3000	[53]
SynRM	50	60	3000	[54]
PMSM	26	36	3744	[52]
SHM	208	1	624	[43]

**TABLE IV Traction Motor Operating Points**

Operating point number	Torque, N·m	Rotational speed, rpm	Mechanical power, kW
1	883	4000	370
2	2793	1265	370
3	8833	400	370

authors interrupt the search after only 26 iterations. At the same time, other studies on optimization using DE [53], [54] show that, in order to find a sufficiently accurate minimum, DE usually requires several times more iterations and the population size. Therefore, it can be assumed that with the continuation of the search, the value of the objective function could be significantly reduced. At the same time, to solve a similar optimization problem for an SHM and an equivalent cycle of 3 operating points, NM required only 208 function calls and 624 motor calculations [43].

**V. PARAMETERS AND OBJECTIVES OF THE IM OPTIMIZATION**

The operation points at which the performance of the SHM and the IM are compared are shown in Table IV.

Operating at point 1 at 4000 rpm, the motor runs at the lowest torque but highest electrical frequency of the fundamental current. This operational state also results in significant losses, with maximum steel losses and AC losses in the winding due to eddy currents. On the other hand, operating point 3, which occurs at a speed of 400 rpm, is characterized by the minimum fundamental electrical frequency and maximum copper loss and armature current. The evaluation of motor performance often revolves around these two points, as they lie on the boundary of the constant power speed region. They provide valuable approximations of the motor's behavior across the entire speed range in the field weakening region, making them crucial reference points for analysis and optimization [65].

In the field of optimizing motor performance at various operational points, the downhill simplex method (Nelder-Mead method) provides a substantial time reduction when compared to population-based techniques like genetic algorithms or particle swarm optimization. This is particularly valuable for multi-point motor performance optimization. Nevertheless, the Nelder-Mead method is a single-criterion unconstrained approach, necessitating a distinct strategy for constructing the objective function in multi-criteria constrained optimization scenarios [66].

Given the resource-intensive nature of the transient 2D mathematical model, this specific approach is chosen for optimization. The performance of the IM is initially assessed at two operational points (points 1 and 3 from Table IV), while point 2 is assessed after the optimization. The optimization objectives focus on average losses  $\langle P_{losses} \rangle$  across points 1 and 3, the maximum current  $\max(I_{arm})$  achieved at point 3 (which corresponds to the maximum torque operating point), and the copper mass  $M$ , considering copper as a high-cost material. These optimization objectives are encapsulated in the objective function expression (11).

The specific torque is not included in the objective function, since the outer dimensions and the loading diagram of the traction motor of the considered off-road vehicle are predefined by the design of the vehicle.

In the optimization process, it is crucial to ensure that the DC voltage  $U_1$  attained at operational point 1 remains below 950 V, allowing a safety margin of 50 V. To achieve all goals described above, the study employs the single criterion Nelder-Mead method. The objective function used is formulated as follows:

$$F = \ln(\langle P_{losses} \rangle) + \ln(I_3) + 0.1 \ln(M) + \dots + 4 \begin{cases} \ln(U_1/950), & \text{when } U_1 > 950 \text{ V;} \\ 0, & \text{otherwise.} \end{cases} \quad (11)$$

Equation (11) comprises two primary terms that signify the balanced importance of reducing average losses and maximum current. It is noteworthy that these objectives are deemed equally valuable in the optimization process. The third term includes copper mass since copper is the most expensive active material. Thus, *ceteris paribus*, preference will be given to a variant with a lower mass of copper in order to make the IM design more economical. The fourth term in the equation establishes a “soft wall”, ensuring compliance with voltage constraints necessary to ensure the high-speed operation. The representation of the geometry of the stator and rotor slots is shown in Fig. 5.

The primary optimization targets encompass the reduction of losses and current within the IM. Consequently, the optimization function assigns equal weightage to the respective terms associated with these objectives. Notably, while decreasing the mass of copper ( $M$ ) is not the primary focus, it is essential to curtail excessive increments in copper mass. To achieve this balance, a logarithmic term  $\ln(M)$  is introduced

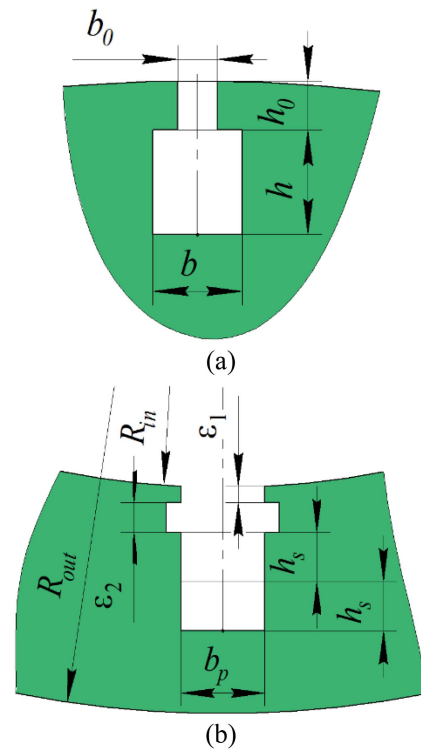


FIGURE 5. Parameters of the IM. (a) Rotor; (b) stator.

TABLE V Unchangeable IM Parameters

Parameter	Value
Stack length $L$ , mm	400
Stator stack outer radius $R_{out}$ , mm	334
Number of poles	8
Wedge thickness $\epsilon_2$ , mm	2
Thickness of unfilled stator slot area $\epsilon_1$ , mm	3
Number of turns in the stator slot	7
Number of parallel branches	2
Rotor tooth tip width $(b - b_0)/2$ , mm	1
Depth of unfilled rotor slot area $h_0$ , mm	5
Specific conductivity of stator winding wire and rotor squirrel cage, MS/m	45

into the equation, carrying a weightage factor of 0.1. This logarithmic factor serves to encourage designs with lower copper mass while maintaining similar loss and current values. Furthermore, the presence of this term effectively constrains the expansion of the rotor’s squirrel cage end ring cross-section, preventing it from growing indefinitely.

Tables V and VI show the parameters that remain fixed and those that are subject to variation during the optimization process. The dimensions of the rectangular winding, crucial for loss calculations, are determined as it is explained in [44].

To simplify the optimization process, the rotor yoke thickness matches that of the stator yoke, and the inner radii of both the rotor laminated stack and squirrel-cage end ring coincide.

Several parameters govern the adjustment of the simulated transient process:  $\alpha$  is set at 1.5 A/W,  $m_0$  is 1500, and  $\gamma$



**TABLE VI** Variable IM Optimization Parameters

Parameter	Initial design	After optimization
Inner stator radius $R_{inners}$ , mm	243	248.8
Stator slot width $b_p$ , mm	9	8.83
Height of winding layer $h_s$ , mm	11	14.6
Air gap, mm	4	3.43
Rotor rod thickness $b$ , mm	9	8.56
Rotor rod height $h$ , mm	20	22.2
Squirrel cage end ring thickness, mm	20	21.6
Slip at point 1, %	1	1.01
Slip at point 2, %	2	2.48
Inner stator radius $R_{inners}$ , mm	243	248.8

\* Note: the current angle at loading point 2 is assumed to be equal to the average of those at loading points 1 and 2.

stands at 1.5. This fictitious transient process extends over 6.8 and 4.8 electric periods of rotor rotation before yielding to an ordinary transient process ( $m = 1$ ) for 1.2 electric periods. In post-processing, the latter half of the rotor's electric rotation periods is utilized to compute motor performance. The time step for discretization is fixed at 0.01 periods of rotor rotation.

## VI. COMPARISON OF THE IM CHARACTERISTICS BEFORE AND AFTER THE OPTIMIZATION

To optimize the induction motor,  $k = 141$  calls to the optimization function were made. Since two operating points are computed for each call to the optimization function, the total number of the time domain IM simulations was  $141 \cdot 2 = 282$  times. These calculations took about 100 hours using a dual core laptop with a 3.0 GHz processor and 192 GB of RAM.

The comparison of the IM performance before and after optimization, carried out according to the methodology presented in the previous section, is presented in Table VII. Mechanical losses consisting of bearing and windage losses is taken as in [44]. Figs. 6 and 7 show the calculated flux density magnitude of the IM before and after optimization.

Initially, in operation point 1, the line-to-line voltage amplitude is set slightly below 950V and is subsequently optimized to precisely match this value. The computation of squirrel cage losses, denoted as  $P_2 \cdot s / (1 - s)$ , through slip and mechanical power  $P_2$ , reveals a marginally lower value compared to the one derived from the FEM model. This discrepancy suggests that any additional cage losses primarily attributed to parasitic harmonics in the airgap remain minimal. This outcome is likely attributed to sufficient airgap dimensions and adequate unfilled space within the rotor slots, which collectively curb the impact of these harmonics.

The power required by the inverter, evaluated as:

$$S_{inv} = (3 \times \sqrt{3} \times V_1 \times I_3) / 2, \quad (12)$$

where  $V_1$  is the line-to-line voltage amplitude at operating point 1;  $I_3$  is the amplitude of the armature phase current at

**TABLE VII** Comparison of Performances of the Induction Motor Before and After Optimization

Parameter	Before optimization		After optimization	
	1	3	1	3
Operating point $i$	1	3	1	3
Rotational speed $n$ , rpm	4000	400	4000	400
Amplitude of the armature phase current $I_{arm}$ , A	223	495	226	416
Efficiency $\eta$ , %	91.04	84.66	91.1	90.1
Output mechanical power $P_2$ , kW	370	370	370	370
Input active power $P_1$ , kW	407	437	406	411
Mechanical loss $P_{mech}$ , kW	17.57	0.05	17.57	0.05
Armature DC copper loss $P_{arm DC}$ , kW	11.42	56.35	8.47	28.56
Armature eddy current copper loss $P_{arm AC}$ , kW	1.37	0.16	2.79	0.15
Stator lamination loss $P_{iron st}$ , kW	1.59	2.65	2.39	2.39
Rotor lamination loss $P_{iron rt}$ , kW	0.48	0.07	0.87	0.07
Squirrel cage losses $P_{sc}$ , kW	3.98	7.82	4.05	9.62
Squirrel cage losses through slip $P_{sc}'$ , kW	3.74	7.56	3.79	9.42
Total loss $P_{loss}$ , kW	36.41	67.10	36.14	40.84
Average losses over points 1 and 3 $\langle P_{loss} \rangle$ , kW	51.76		38.49	
Power factor	0.77	0.61	0.72	0.75
Line-to-line voltage amplitude $V_{arms}$ , V	909	557	948	508
Torque ripple, %	4.3	1.8	7.0	2.7
Required inverter power $S_{inv}$ , MVA	1.17		1.024	

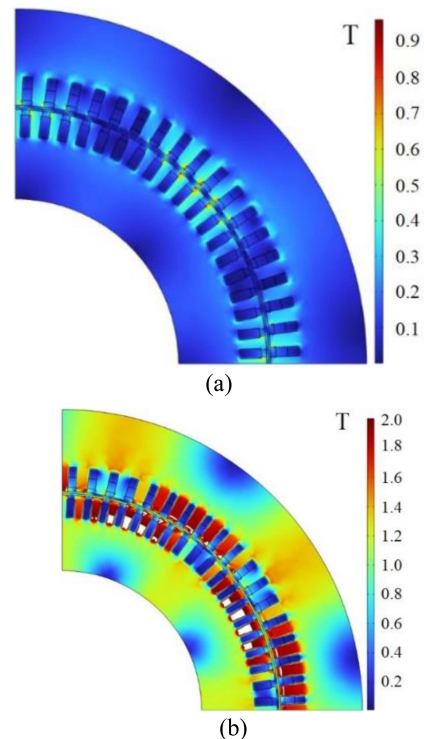


**FIGURE 6.** The cross-section of the initial design of the induction motor and the magnitude plot of flux density; white areas mark the extreme saturation level (more than 2 T): (a) Loading point 1 (maximum speed); (b) Loading point 3 (maximum torque).

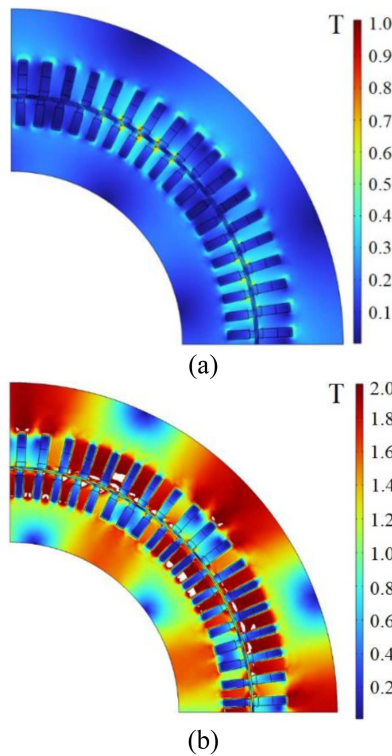


**FIGURE 7. The cross-section and flux density magnitude of the optimized induction motor; extreme saturation (more than 2 T) marked in white. (a) Loading point 3 (maximum speed); (b) Loading point 1 (maximum torque).**

operating point 3. A factor of 3 is added to the formula since a 9-phase inverter is considered, which can be divided into three three-phase inverters.

It notably reduced by approximately  $100\%(1.17 - 1.024)/1.17 = 11\%$ .

Over operation points 1 and 3, the average losses undergo a significant reduction, primarily stemming from a remarkable decrease in armature DC losses by factors of 2.8 and 3.8 in points 1 and 3, respectively. The decrease in airgap dimensions and the mitigation of rotor teeth saturation in point 3 further aid in minimizing armature DC losses. However, it's important to note that reducing the airgap dimensions also introduces the challenge of parasitic harmonics, leading to amplified core losses and eddy current losses within the armature winding. Additionally, squirrel cage losses experience an increase, likely attributed to higher slip values in both operating modes.

### VII. COMPARATIVE ANALYSIS OF OPTIMIZED CHARACTERISTICS: SHM VERSUS IM

In this section, a comprehensive comparison is presented, examining the characteristics of the electrical machines under consideration after the optimization process. Performance comparison of the optimized designs for both the SHM and IM is provided in Table VIII and in Fig. 8. The optimized

**TABLE VIII Comparison of Optimized Characteristics: IM Versus SHM**

Parameter	SHM			IM		
	1	2	3	1	2	3
Operating point $i$	1	2	3	1	2	3
Rotational speed $n$ , rpm	4000	1265	400	4000	1265	400
Amplitude of the armature phase current $I_{arms}$ , A	176	255	601	226	215	416
Motor efficiency $\eta$ , %	90.5	96.1	90.1	91.1	96.22	90.1
Output mechanical power $P_2$ , kW	370	370	370	370	370	370
Input active power $P_1$ , kW	408	384	399	406	384	411
Mechanical loss $P_{mech}$ , kW	17.57	0.65	0.05	17.57	0.65	0.05
Armature DC copper loss $P_{arm DC}$ , kW	2.1	4.5	25.0	8.47	7.60	28.56
Armature eddy current copper loss $P_{arm AC}$ , kW	6.0	2.1	1.0	2.79	0.36	0.15
Stator lamination loss $P_{iron st}$ , kW	10.9	5.9	2.5	2.39	2.98	2.39
Rotor lamination loss $P_{iron rt}$ , kW	1.5	0.6	0.1	0.87	0.25	0.07
Excitation copper loss for SHM $P_{exc}$ , kW	0.5	1.5	11.9	-	-	-
Squirrel cage losses for IM $P_{sc}$ , kW	-	-	-	4.05	2.69	9.62
Total loss $P_{loss}$ , kW	38.7	15.2	40.5	36.14	14.54	40.84
Power factor	0.97	0.96	0.96	0.72	0.77	0.75
Line-to-line voltage amplitude $V_{arms}$ , V	988	632	275	948	895	508
Torque ripple, %	18.9	12.5	3.0	7.0	6.5	2.7

Notes: \* The IM efficiency is calculated as  $\eta = P_2/P_1 = P_2/(P_2 + P_{loss})$ , the SHM efficiency is calculated as  $\eta = P_2/(P_1 + P_{exc}) = P_2/(P_2 + P_{loss})$  where  $P_1$  is the active power in armature winding;  $P_{exc}$  is the loss in the excitation winding;  $P_{mech}$  is the output (mechanical) power.

\*\* The total loss for IM is calculated as the sum of the following  $P_{loss} = P_{arm DC} + P_{arm AC} + P_{mech} + P_{iron st} + P_{iron rt} + P_{sc}$ ; the total loss for SHM is calculated as the sum of the following  $P_{loss} = P_{arm DC} + P_{arm AC} + P_{mech} + P_{iron st} + P_{iron rt} + P_{exc}$ .

performance attributes of the IM outlined in Table VIII for operational points 1 and 3 mirror those depicted in Table VII. For operational point 2, the optimized IM characteristics are computed utilizing slip values of 1.3%, 1.4%, and 1.5%. Among these, the results associated with a slip of 1.4%, demonstrating the lowest total losses, are highlighted in Table VIII. Table IX compares the masses and dimensions of the SHM and the IM. The article [43] provides a comprehensive description of the design methods and detailed results pertaining to the SHM.

\*\* The total loss for IM is calculated as the sum of the following  $P_{loss} = P_{arm DC} + P_{arm AC} + P_{mech} + P_{iron st} + P_{iron rt} + P_{sc}$ ; the total loss for SHM is calculated as the sum of the following  $P_{loss} = P_{arm DC} + P_{arm AC} + P_{mech} + P_{iron st} + P_{iron rt} + P_{exc}$ .

Comparing the parameters of the IM and SHM and their characteristics shown in Table VIII and Table IX, we can draw the following conclusions:

- 1) Losses in the IM and SHM are roughly comparable. The IM loss is less than that of the SHM by  $100\% \cdot (38.7 - 36.14)/38.7 = 6.6\%$  at operating point 1 at maximum speed. The IM loss is less than the of the SHM by  $100\% \cdot (15.2 - 14.54)/15.2 = 4.3\%$  at operating point 2. the SHM loss is less than the IM loss by  $100\% \cdot (40.84 - 40.5)/40.84 = 0.8\%$  at operating point 3 with maximum torque;

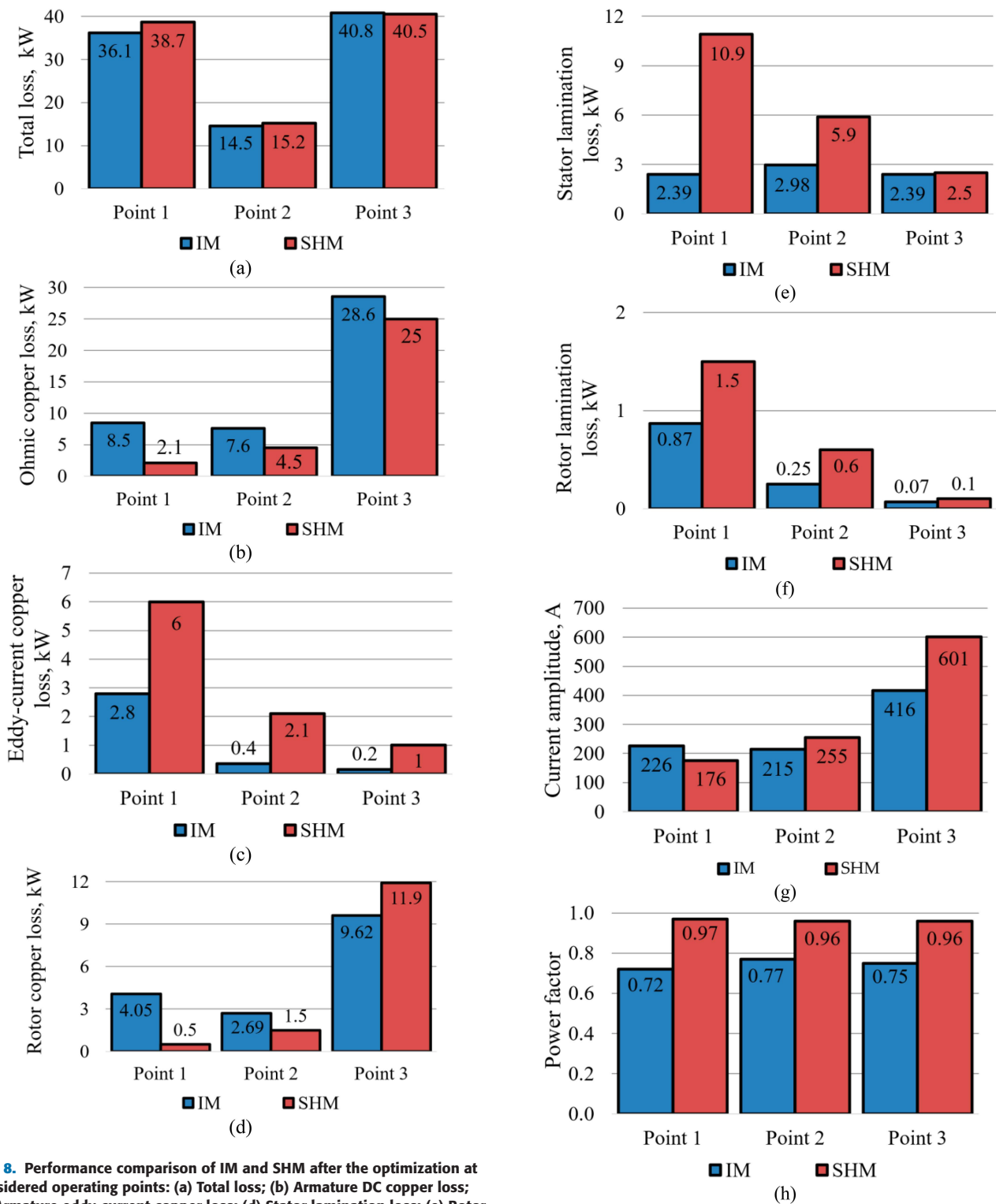


**FIG. 8.** Performance comparison of IM and SHM after the optimization at considered operating points: (a) Total loss; (b) Armature DC copper loss; (c) Armature eddy-current copper loss; (d) Stator lamination loss; (e) Rotor lamination loss; (f) Rotor excitation/squirrel cage copper loss; (g) Amplitude of the armature phase current; (h) Power factor.

**FIG. 8.** Continued.

- The length of the stator without taking into account the winding end parts of IM is less than that of SHM by 100%  $(545 - 400)/545 = 26.6\%$ ;
- The mass of active materials of the IM is less than that of the SHM by 100%  $(1003 - 817)/1003 = 18.5\%$ . At

the same time, the cost of the SHM active materials is lower by 100%  $(1807 - 1531)/1807 = 15.3\%$  due to the lower use of copper due to the compact size of the annular coils of the excitation winding [43]. Therefore, the SHM excitation winding requires  $88/20 = 4.4$  times less

**TABLE IX Comparison of Masses, Costs, and Some Dimensions of the Optimized SHM and IM**

Parameter	SHM	IM
Stator lamination mass, kg	320	410
Rotor lamination mass, kg	231	242
Armature copper mass, kg	68	77
Excitation/squirrel cage copper mass, kg	20	88
Weight of low carbon steel of stator housing, kg	182	-
Weight of low carbon steel of rotor sleeve, kg	182	-
Total mass of the rotor materials, kg	433	330
Total mass of laminations, copper, and low carbon steel, kg	1003	817
Stator lamination cost, USD	320	410
Rotor lamination cost, USD	231	242
Armature copper cost, USD	476	539
Excitation/squirrel cage copper cost, USD	140	616
Low carbon steel cost, USD	364	-
Total cost of laminations, copper, and low carbon steel, USD*	1531	1807
Total length of the stator lamination, mm	431	400
Total length of the stator excluding the winding end parts (including spaces for the excitation coils for SHM), mm	545	400
Total length of the machine including the winding end parts, mm	711	649
Stator lamination outer diameter, mm	668	668
Air gap, mm	2.4	3.43

\* Note: the following material costs are assumed: copper—USD 7/kg, steel—USD 1/kg [67].

copper than the rotor short-circuited winding on the IM rotor. The SHM armature winding also requires  $77/68 = 1.13$  times less copper than the IM stator winding. In total, the SHM requires  $(88+77)/(20+68) = 165/88 = 1.87$  times less copper;

- 4) The assembly technology of the SHM is somewhat more complicated than that of the IM, but the cost of active materials of the SHM is lower than for the IM (see Table IX). In addition, the SHM does not require the manufacture of a copper short-circuited cage on the rotor. Therefore, the cost of the SHM is approximately equal to the cost of the IM;
- 5) It should also be noted that SHM has increased reliability due to the absence of a rotor winding and the risk of breaking its rod or breaking the contact between the short-circuit ring and the rod.

### VIII. INVERTER POWER LOSS AND TEMPERATURE RIPPLE FOR THE IM AND SHM

The analysis presented in this section sheds light on the contrasting aspects of the thermal behavior and efficiency of semiconductor power switches when using two types of motors, highlighting the potential advantages of the SHM design in specific operating scenarios.

Inverter power modules are one of the most expensive parts of a traction drive, so reducing their cost will greatly increase the economic attractiveness of the solution. Cost reduction can be achieved by reducing the maximum phase current of the motor and, accordingly, the rated current of the inverter, which was carried out within the framework of this study using computer-aided optimization. However, when choosing the rated current of the inverter, it is not enough to take into account the maximum value of the fundamental component of the motor current. It is also necessary to leave some current margin in case of inaccuracies in the calculation of the theoretical characteristics of the motor and powertrain (e.g. the torque-speed characteristic shown in Fig. 4), which always take place due to the complexity of these systems. In addition, when choosing a power module, it is necessary to consider the operating conditions that negatively affect its service life [23], [68]. As highlighted above, one of these significant negative effects is the thermocycling of the power switches of the traction inverter when the vehicle is parked on a slope when using an induction motor. In this case, large-amplitude low-frequency phase current ripples lead to corresponding temperature ripples in the inverter power modules [48].

Taking into account these factors, in practice, power modules are selected with a large margin. In [20], for a drive of a 240-ton mining dump truck, it is shown that although the maximum phase current of the motor is only 1500 A, a power module SKiP-4 with a rating of 3600 A is selected, probably for a general increase in reliability, in particular, taking into account the debilitating impact of thermal cycling. By analogy, the inverter power module FF650R17IE4 with the current rating of 650 A was chosen with double margin for the IM (considering the maximum IM current is 325 A, as shown in Table VIII).

Based on the same principle, for the SHM with a maximum current of 601 A (see Table VIII), we choose the FF1000R17IE4 power module. It should be noted that the SHM offers a significant advantage during electric brake mode, particularly when halting on an incline. In an IM, the presence of slip gives rise to considerable temperature fluctuations, leading to adverse effects on the longevity of inverter switches. However, in SHM, under such loading conditions, direct currents traverse the phases, effectively eradicating temperature fluctuations.

To provide a comprehensive comparison between SHM and IM, let us examine losses, temperature levels, and temperature fluctuations in inverter switches at the operating point with maximum torque ( $i = 3$ ). Loss calculations for the inverter were performed using IPOSIM software [69], utilizing motor current and voltage data along with power module characteristics obtained. The calculation was made for the three-phase part of the 9-phase inverter circuit shown in Fig. 3, assuming that the processes are symmetrical in the phases not included in the calculation. Table X presents a contrast in the inverter temperature ripples between the SHM and IM at maximum torque and a speed of 400 rpm. When calculating losses in the inverter, it is assumed that

**TABLE X** Inverter Losses and Temperature Ripple Evaluation of the SHM and IM At 400 Rpm

Parameter	SHM	IM
IGBT module	FF1000R17IE4	FF650R17IE4
PWM frequency $f_{PWM}$ , Hz	2000	1333.3
DC link voltage $V_{DC}$ , V	950	
Fundamental frequency $f$ , Hz*	26.6	27.3
RMS phase current, A	425	294.2
Amplitude of fundamental line-to-line voltage $V_{ams}$ , V	275	508
Modulation index $k_m = V_{ams}/V_{DC}$	0.289	0.535
Power factor	0.96	0.75
Switching loss (IGBT), W	217.33	113.42
Switching loss (freewheeling diode), W	85.95	38.25
Conduction loss (IGBT), W	181.17	139.84
Conduction loss (freewheeling diode), W	106.66	64.07
Total loss (IGBT), W	398.5	253.26
Total loss (freewheeling diode), W	192.61	102.32
Maximum/minimum temperature (IGBT), °C	65.3/61.2	65.47/60.2
Maximum/minimum temperature (freewheeling diode), °C	65.3/60.2	63.16/57.8
Temperature ripple (IGBT), °C	4.1	5.3
Temperature ripple (freewheeling diode), °C	5.1	5.3

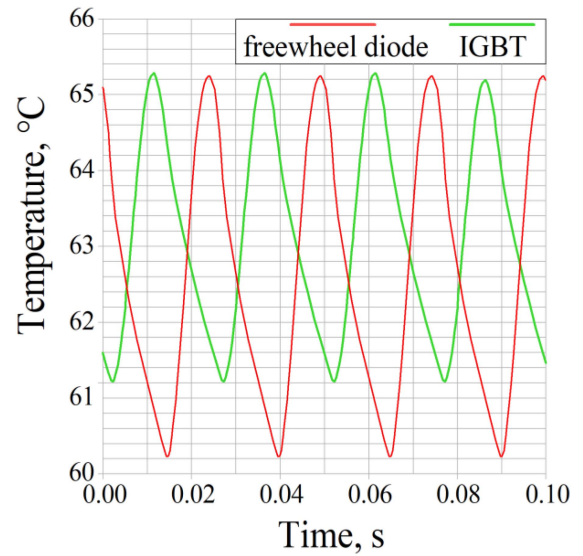
\* Note: The fundamental supply frequency  $f$  is given by  $(n \times p)/60 + f_s$ , where  $p$  represents the motor's pole number,  $n$  is the rotational speed in rpm, and  $f_s$  denotes the slip frequency.

the PWM frequency  $f_{PWM}$  is proportional to the number of motor poles. The current, voltage and power factor for calculation are taken from the motor performance calculation results shown in Table VII. The values of switching loss and conduction loss are calculated separately for one IGBT and one freewheeling diode. The ambient temperature for thermal calculations is assumed to be 50°C. Fig. 9 visually presents the temperature ripple in the inverter switch components for this scenario.

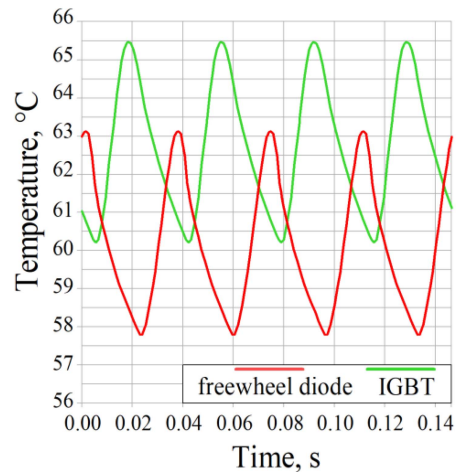
The IGBT and freewheeling diode experience periodic temperature variations over time, leading to a significant amplitude that adversely impacts their lifespan. At 400 rpm, the maximum temperatures of the freewheeling diode and IGBT, as well as their temperature ripple, are approximately equal for the SHM and IM. Table XI compares inverter loss and temperature between the SHM and IM at peak torque and zero speed (electric braking during slope stop). Fig. 10 shows the temperature profiles for this case.

Let us proceed to a comparison of the inverter utilization factor, denoted as  $K_i = P_2/S$ . This factor signifies the ratio between the mechanical output power of the electric drive and the rated apparent power of the inverter, computed according to [44]. For the IM, employing the FF650R17IE4 power module ( $V_{DC} = 1000$  V,  $I_{Cnom} = 650$  A), the  $K_i$  value is calculated as

$$K_i = 370,000 / (9 \times 1000 \times 650) / (2 \cdot \sqrt{3}) = 0.219.$$



(a)



(b)

**FIGURE 9.** The temperature profiles of inverter components during motor operation over time. The IGBT temperature is represented by the green line, and the freewheeling diode temperature is indicated by the red line. (a) SHM at 400 rpm employing FF1000R17IE4 modules; (b) IM at 400 rpm employing FF650R17IE4 modules.

In the case of the SHM, utilizing the FF1000R17IE4 power module ( $V_{DC} = 1000$  V,  $I_{Cnom} = 1000$  A), the  $K_i$  value is determined as

$$K_i = 2 \cdot \sqrt{3} \cdot 370,000 / (9 \times 1000 \times 1000) = 0.142,$$

with a notable difference between the two systems.

The FF650R17IE4 module is priced at USD 612, while the FF1000R17IE4 module costs USD 868 [70]. Each module consists of 2 power switches (1 phase), and a total of 9 modules are required to power a 9-phase motor. Consequently, the overall cost of inverter power modules for the induction motor (IM) amounts to  $9 \cdot 612 =$  USD 5508. On the other hand, for the synchronous homopolar motor (SHM), the cost of inverter power modules comes to  $9 \cdot 868 =$  USD 7812. Therefore, when

**TABLE XI** Inverter Losses and Temperature Ripple Evaluation of the SHM and IM At 0 Rpm (Full Electric Brake)

Parameter	SHM	IM
IGBT module	FF1000R17IE4	FF650R17IE4
PWM frequency $f_{PWM}$ , Hz	2000	1333.3
DC link voltage $V_{DC}$ , V	950	
Fundamental frequency $f = (n \times p)/60$ , Hz	0	0.7
RMS phase current, A	425	294.2
Modulation index $k_m = V_{arm}/V_{DC}$	0.025	0.038
Power factor	1	0.97
Switching loss (IGBT), W	950	117.3
Switching loss (freewheeling diode), W	0	41.6
Conduction loss (IGBT), W	846	108.6
Conduction loss (freewheeling diode), W	0	94.4
Total loss (IGBT), W	1796	225.9
Total loss (freewheeling diode), W	0	136.1
Maximum/minimum temperature (IGBT), °C	93/93	78/52
Maximum/minimum temperature (freewheeling diode), °C	50/50	84/53
Temperature ripple (IGBT), °C	0*	26
Temperature ripple (freewheeling diode), °C	0*	31

Note: \*At zero speed, the absence of temperature ripple occurs in the SHM when powered, attributed to DC currents flowing through the phase windings. Conversely, in the IM, a non-zero temperature ripple persists due to the presence of slip frequency currents in the phase windings.

utilizing the SHM instead of the IM, the cost of power modules is  $7812/5508 = 1.41$  times higher.

At the same time, incorporating the SHM enhances inverter reliability, particularly evident when halting on inclines. Unlike the IM, which experiences a substantial low-frequency temperature fluctuation of around 30 °C, SHM operation avoids this issue. This advantage systems from the absence of large low-frequency temperature ripples in SHM’s traction inverter power modules, as highlighted in Table XI.

**IX. DISCUSSION**

Based on the comparative theoretical analysis carried out, we can conclude that the advantage of the IM over the SHM is somewhat lower power loss. As shown above, the IM loss is less than that of the SHM by 6.6% at operating point 1 at the maximum speed. Also, the IM loss is less than that of the SHM by 4.3% at operating point 2 at the intermediate speed. The SHM loss is less than that of the IM by 0.8 % at operating point 3 with the maximum torque. In addition, the length of the stator core without taking into account the winding end parts of the IM is less than that of the SHM by 26.6%.

The mass of active materials of the IM is 18.5% less due to the massive stator housing and rotor sleeve of the SHM. At the same time, the cost of the SHM active materials is lower by 15.3% because of less use of copper due to the compact size of the ring coils of the field winding. The compact SHM field winding requires 4.4 times less copper than the short-circuited rotor winding on the IM. The SHM armature winding also

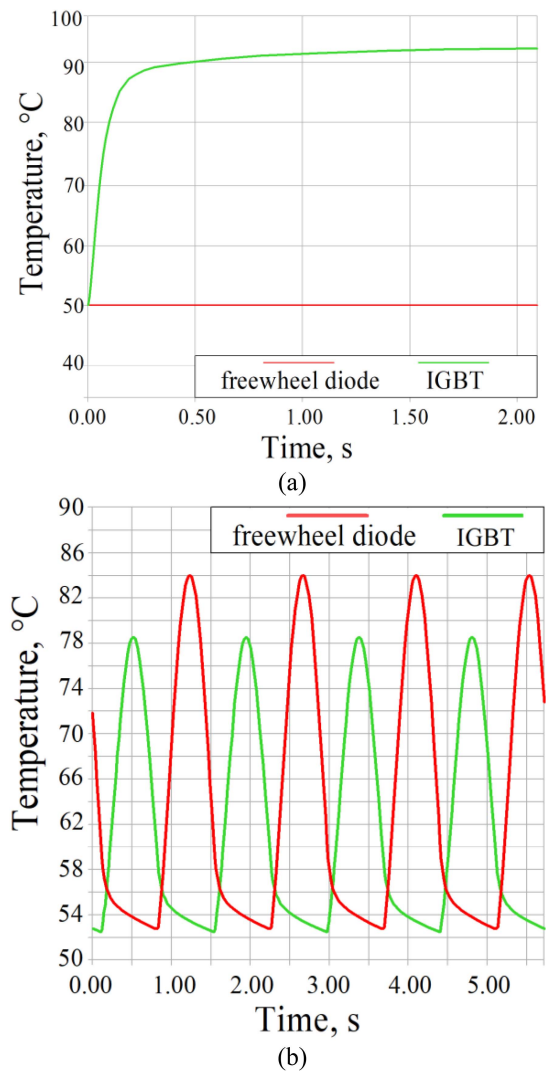


**FIG. 10.** The temperature profiles of inverter components during motor operation over time. The IGBT temperature is represented by the green line, and the freewheeling diode temperature is indicated by the red line. (a) SHM at 0 rpm employing FF1000R17IE4 modules; (b) IM at 0 rpm employing FF650R17IE4 modules.

requires 1.13 times less copper than the IM stator winding. In total, the SHM requires 1.87 times less copper.

Thus, losses in the IM are reduced to 6.6%, the length of the laminated magnetic core is 26.6% less, and the mass of the core is 18.5% less. Although the SHM has a 15.3% lower cost of active materials.

Additionally, unlike IM, whose inverter power switches are subject to significant low-frequency temperature ripples (about 30°C peak-to-peak) when stopped on a slope, SHM avoids this problem, which improves reliability.

**X. CONCLUSION**

The article theoretically compares the performance of the optimized SHM and IM designs in a 370 kW mining truck drive, with CPSR 10:1400-4000 rpm).

When quantitatively comparing their characteristics, no clear favorite was identified: the characteristics of the IM and SHM are approximately comparable.

When using the SHM, the cost of the inverter power modules is 1.41 times more than when using the IM. However, the advantage of a traction drive based on the SHM over the IM is greater reliability, provided by the absence of a rotor winding and the risk of breaking its rod or breaking contact between the short-circuiting ring and the rod. In addition, when using the SHM, greater reliability of the traction solid-state inverter is provided due to the absence of a large temperature ripple in the power modules in the electric braking mode when stopped on a slope, often used in the considered application.

## REFERENCES

- [1] A. Dianov, "Instant closing of permanent magnet synchronous motor control systems at open-loop start," *Sustainability*, vol. 14, 2022, Art. no. 12665, doi: [10.3390/su141912665](https://doi.org/10.3390/su141912665).
- [2] R. Schulze, "Reducing environmental impacts of the global rare earth production for use in Nd-Fe-B magnets, how magnetic technologies much can recycling contribute?" Ph.D. dissertation, Dept. Civil Environ. Eng., Tech. Univ. Darmstadt, Darmstadt, Germany, Dec. 2018. Accessed: Jul. 19, 2024. [Online]. Available: <https://tprints.ulb.tu-darmstadt.de/8301/7/Diss%20Rita%20Schulze%2015-12-2018.pdf>
- [3] S. Dong, W. Li, H. Chen, and R. Han, "The status of Chinese permanent magnet industry and R&D activities," *AIP Adv.*, vol. 7, pp. 1–17, 2017, doi: [10.1063/1.4978699](https://doi.org/10.1063/1.4978699).
- [4] "The net-zero materials transition: Implications for global supply chains," Report, McKinsey &, Jul. 2023. Accessed: Sep. 18, 2023, [Online]. Available: <https://www.mckinsey.com/industries/metals-and-mining/our-insights/the-net-zero-materials-transition-implications-for-global-supply-chains>
- [5] V. Dmitrievskii, V. Prakht, and V. Kazakbaev, "Synchronous reluctance generator with ferrite magnets for wind turbine," *J. Phys.: Conf. Ser.*, vol. 1102, 2018, Art. no. 012041, doi: [10.1088/1742-6596/1102/1/012041](https://doi.org/10.1088/1742-6596/1102/1/012041).
- [6] W. I. B. De Lima, *Rare Earth Industry*. Amsterdam, The Netherlands: Elsevier, 2015.
- [7] V. Dmitrievskii, V. Prakht, V. Kazakbaev, and A. Anuchin, "Comparison of interior permanent magnet and synchronous homopolar motors for a mining dump truck traction drive operated in wide constant power speed range," *Mathematics*, vol. 10, 2022, Art. no. 1581, doi: [10.3390/math10091581](https://doi.org/10.3390/math10091581).
- [8] W. Koellner, G. Brown, J. Rodriguez, J. Pontt, P. Cortes, and H. Miranda, "Recent advances in mining haul trucks," *IEEE Trans. Ind. Electron.*, vol. 51, pp. 321–329, Apr. 2004, doi: [10.1109/TIE.2004.825263](https://doi.org/10.1109/TIE.2004.825263).
- [9] A. Fathy Abouzeid et al., "Control strategies for induction motors in railway traction applications," *Energies*, vol. 13, 2020, Art. no. 700, doi: [10.3390/en13030700](https://doi.org/10.3390/en13030700).
- [10] J. Bernatt, S. Gawron, T. Glinka, and A. Polak, "Traction induction motor," in *Proc. 13th Int. Conf. Modern Electrified Transport*, Warsaw, Poland, Oct. 5-7, 2017, pp. 1–5, doi: [10.1051/mateconf/201818004005](https://doi.org/10.1051/mateconf/201818004005).
- [11] B. Kim et al., "Development of 50kW traction induction motor for electric vehicle (EV)," in *Proc. IEEE Veh. Power Propulsion Conf.*, 2012, pp. 142–147, doi: [10.1109/VPPC.2012.6422627](https://doi.org/10.1109/VPPC.2012.6422627).
- [12] S. A. Mansouri, A. Ahmarinejad, M. S. Javadi, R. Heidari, and J. P. Catalao, "Improved double-surface sliding mode observer for flux and speed estimation of induction motors," *IET Electric Power Appl.*, vol. 14, no. 6, pp. 1002–1010, 2020, doi: [10.1049/iet-epa.2019.082](https://doi.org/10.1049/iet-epa.2019.082).
- [13] J. Doerr et al., "The electric drivetrain with three-motor layout of the Audi E-tron S," *MTZ Worldwide*, vol. 81, pp. 16–25, 2020, doi: [10.1007/s38313-020-0254-2](https://doi.org/10.1007/s38313-020-0254-2).
- [14] M. Popescu, J. Goss, D. Staton, D. Hawkins, Y. Chong, and A. Boglietti, "Electrical vehicles-practical solutions for power traction motor systems," *IEEE Trans. Ind. Appl.*, vol. 54, no. 3, pp. 2751–2762, May/Jun. 2018, doi: [10.1109/TIA.2018.2792459](https://doi.org/10.1109/TIA.2018.2792459).
- [15] K. Matsuoka and M. Kondo, "Energy saving technologies for railway traction motors," *IEEE Trans. Elect. Electron. Eng.*, vol. 5, pp. 278–284, 2010, doi: [10.1002/tee.20530](https://doi.org/10.1002/tee.20530).
- [16] A. T. De Almeida, F. J. Ferreira, and G. Baoming, "Beyond induction motors-technology trends to move up efficiency," *IEEE Trans. Ind. Appl.*, vol. 50, no. 3, pp. 2103–2114, May/Jun. 2014, doi: [10.1109/TIA.2013.2288425](https://doi.org/10.1109/TIA.2013.2288425).
- [17] L. Fedoseyev and E. Marcum Pearce, Jr., "Rotor assembly with heat pipe cooling system," U.S. Patent US9331552B2, 2013. Accessed: Jul. 19, 2024. [Online]. Available: <https://patents.google.com/patent/US9331552B2/en?q=US9331552B2>
- [18] Z. Zhu, W. Chu, and Y. Guan, "Quantitative comparison of electromagnetic performance of electrical machines for HEVs/EVs," *CES Trans. Elect. Machines Syst.*, vol. 1, no. 1, pp. 37–47, 2017, doi: [10.23919/TEMS.2017.7911107](https://doi.org/10.23919/TEMS.2017.7911107).
- [19] A. Vinogradov, A. Sibirtsev, N. Gnezdov, V. Chistoserdov, and A. Korotkov, "Control algorithms and technical solutions in the traction electrical drive of mining dump trucks," *Elektrichestvo*, vol. 2, pp. 60–68, 2023, (In Russian), doi: [10.24160/0013-5380-2023-2-60-68](https://doi.org/10.24160/0013-5380-2023-2-60-68).
- [20] A. Vinogradov, V. Chistoserdov, and A. Sibirtsev, "Sets of traction electrical equipment for heavy-duty mining dump trucks," Accessed: Sep. 18, 2023. (In Russian). [Online]. Available: [http://vectorgroup.ru/articles/DP\\_2017\\_1](http://vectorgroup.ru/articles/DP_2017_1)
- [21] S. Hiti, D. Tang, C. Stancu, and E. Ostrom, "Zero vector modulation method for voltage source inverter operating near zero output frequency," in *Proc. IEEE Ind. Appl. Conf., 39th IAS Annu. Meeting*, 2004, pp. 171–176, doi: [10.1109/IAS.2004.1348404](https://doi.org/10.1109/IAS.2004.1348404).
- [22] B. Cougo, L. M. F. Morais, G. Segond, R. Riva, and H. Tran Duc, "Influence of PWM methods on semiconductor losses and thermal cycling of 15-kVA three-phase SiC inverter for aircraft applications," *Electronics*, vol. 9, 2020, Art. no. 620, doi: [10.3390/electronics9040620](https://doi.org/10.3390/electronics9040620).
- [23] Y. Ali, E. Kulik, A. Anuchin, and D. H. Do, "Thermal cycling effect in a traction inverter for star-connected and open-end winding permanent magnet synchronous motors with nearly constant losses current regulation," in *Proc. IEEE 29th Int. Workshop Electric Drives: Adv. Power Electron. Electric Drives*, 2022, pp. 1–6, doi: [10.1109/IWED54598.2022.9722583](https://doi.org/10.1109/IWED54598.2022.9722583).
- [24] "How to finesse and etron on an incline and parallel parking? AudiWorld forum," Accessed: Sep. 18, 2023. [Online]. Available: <https://www.audiworld.com/forums/audi-e-tron-q8-e-tron-232/how-finesse-etron-incline-parallel-parking-3018036/>
- [25] "Tesla motor designer explains Model 3's transition to permanent magnet motor. Press release," Accessed: Sep. 18, 2023. [Online]. Available: <https://advancedmagnetsource.com/2022/06/15/tesla-motor-designer-explains-model-3s-transition-to-permanent-magnet-motor/>
- [26] Audi equips Q4 Sportback e-tron with PM and induction motors. Press release," Accessed: Sep. 18, 2023. [Online]. Available: <https://www.automotivepowertraintechologyinternational.com/news/new-engine/audi-equips-q4-sportback-e-tron-with-pm-and-induction-motors.html>
- [27] R. J. Thompson and A. T. Visser, "Benchmarking and management of fugitive dust emissions from surface-mine haul roads," *Mining Technol.*, vol. 111, no. 1, pp. 28–34, 2002, doi: [10.1179/mnt.2002.111.1.28](https://doi.org/10.1179/mnt.2002.111.1.28).
- [28] V. Dmitrievskii, V. Prakht, E. Valeev, A. Paramonov, V. Kazakbaev, and A. Anuchin, "Comparative study of induction and wound rotor synchronous motors for the traction drive of a mining dump truck operating in wide constant power speed range," *IEEE Access*, vol. 11, pp. 68395–68409, 2023, doi: [10.1109/ACCESS.2023.3292244](https://doi.org/10.1109/ACCESS.2023.3292244).
- [29] "The first-ever BMW iX3, PressClub Global," Article. Press kit. 14.07.2020. Accessed: Sep. 18, 2023. [Online]. Available: <https://www.press.bmwgroup.com/global/article/detail/T0310696EN/the-first-ever-bmw-ix3?language=enhttps://www.netcarshow.com/bmw/2021-ix3>
- [30] S. Feustel, B. Huebner, D. Loos, J. Merwerth, Y. Tremaudant, and K. Vollmer, "Rotor for separately excited inner rotor synchronous machine, inner rotor synchronous machine, motor vehicle and method," U.S. Patent US20210006105A1, Jan. 7, 2021. Accessed: Sep. 18, 2023. [Online]. Available: <https://patents.google.com/patent/US20210006105A1>
- [31] M. R. Raia, M. Ruba, C. Martis, C. Husar, and G. M. Sirbu, "Battery electric vehicle (BEV) powertrain modelling and testing for real-time control prototyping platform integration," in *Proc. IEEE 23rd Eur. Conf. Power Electron. Appl.*, Ghent, Belgium, Sep. 6-10, 2021, pp. 1–10, doi: [10.23919/EPE21ECCEurope50061.2021.9570616](https://doi.org/10.23919/EPE21ECCEurope50061.2021.9570616).

- [32] D. Ting, "Renault fluence Z.E. is a positive influence," May 21, 2012. Accessed: Sep. 18, 2023. [Online]. Available: <https://www.torque.com.sg/reviews/renault-fluence-z-e-is-a-positive-influence/>
- [33] G. Jolit and Y. Chenot, "All-new megane e-tech electric: Delving into the heart of innovation," Episode 3 - A patent for an eco-friendlier electric motor, Jul. 25, 2022. Accessed: Sep. 18, 2023. [Online]. Available: <https://media.renault.com/all-new-megane-e-tech-electric-delving-into-the-heart-of-innovation-episode-3/>
- [34] W. Q. Chu et al., "Comparison of electrically excited and interior permanent magnet machines for hybrid electric vehicle application," in *Proc. 17th Int. Conf. Elect. Machines Syst. (ICEMS)*, Hangzhou, China, Oct. 2014, pp. 401–407, doi: [10.1109/ICEMS.2014.7013504](https://doi.org/10.1109/ICEMS.2014.7013504).
- [35] E. Illiano, "Design of a highly efficient brushless current excited synchronous motor for automotive purposes," Ph.D. dissertation, Dept. Mech. Process. Eng., ETH-Zrich, Zrich, Switzerland, 2014, doi: [10.3929/ethz-a-010433793](https://doi.org/10.3929/ethz-a-010433793).
- [36] C. Stancu, T. Ward, K. Rahman, R. Dawsey, and P. Savagian, "Separately excited synchronous motor with rotary transformer for hybrid vehicle application," in *Proc. IEEE Energy Convers. Congr. Expo.*, Pittsburgh, PA, USA, 2014, pp. 5844–5851, doi: [10.1109/ECCE.2014.6954203](https://doi.org/10.1109/ECCE.2014.6954203).
- [37] S. Orlova, V. Pugachov, and N. Levin, "Hybrid excitation of the axial inductor machine," *Latvian J. Phys. Tech. Sci.*, vol. 49, pp. 35–41, 2012, doi: [10.2478/v10047-012-0004-6](https://doi.org/10.2478/v10047-012-0004-6).
- [38] G. Bindu, J. Basheer, and A. Venugopal, "Analysis and control of rotor eccentricity in a train-lighting alternator," in *Proc. IEEE Int. Conf. Power, Control, Signals Instrum. Eng.*, Chennai, India, 2017, pp. 2021–2025, doi: [10.1109/ICPCSI.2017.8392070](https://doi.org/10.1109/ICPCSI.2017.8392070).
- [39] L. Lorilla, T. Keim, J. Lang, and D. Perreault, "Topologies for future automotive generators. Part I. Modeling and analytics," in *Proc. IEEE Veh. Power Propulsion Conf.*, Chicago, IL, USA, 2005, pp. 74–85, doi: [10.1109/VPPC.2005.1554651](https://doi.org/10.1109/VPPC.2005.1554651).
- [40] C. Bianchini, F. Immovilli, A. Bellini, E. Lorenzani, C. Concarì, and M. Scolari, "Homopolar generators: An overview," in *Proc. IEEE Energy Convers. Congr. Expo.*, Phoenix, AZ, USA, 2011, pp. 1523–1527, doi: [10.1109/ECCE.2011.6063962](https://doi.org/10.1109/ECCE.2011.6063962).
- [41] V. Dmitrievskii, V. Prakht, A. Anuchin, and V. Kazakbaev, "Traction synchronous homopolar motor: Simplified computation technique and experimental validation," *IEEE Access*, vol. 8, pp. 185112–185120, 2020, doi: [10.1109/ACCESS.2020.3029740](https://doi.org/10.1109/ACCESS.2020.3029740).
- [42] M. Lashkevich, A. Anuchin, D. Aliamkin, and F. Briz, "Control strategy for synchronous homopolar motor in traction applications," in *Proc. IEEE 43rd Annu. Conf. Ind. Electron. Soc.*, Beijing, China, 2017, pp. 6607–6611, doi: [10.1109/IECON.2017.8217153](https://doi.org/10.1109/IECON.2017.8217153).
- [43] V. Prakht, V. Dmitrievskii, A. Anuchin, and V. Kazakbaev, "Inverter volt-ampere capacity reduction by optimization of the traction synchronous homopolar motor," *Mathematics*, vol. 9, 2021, Art. no. 2859, doi: [10.3390/math9222859](https://doi.org/10.3390/math9222859).
- [44] V. Prakht, V. Dmitrievskii, V. Kazakbaev, and A. Anuchin, "Comparative study of electrically excited conventional and homopolar synchronous motors for the traction drive of a mining dump truck operating in a wide speed range in field-weakening region," *Mathematics*, vol. 10, 2022, Art. no. 3364, doi: [10.3390/math10183364](https://doi.org/10.3390/math10183364).
- [45] H. C. Idoko, U. B. Akuru, R.-J. Wang, and O. Popoola, "Potentials of brushless stator-mounted machines in electric vehicle drives—A literature review," *World Electric Veh. J.*, vol. 13, no. 5, 2022, Art. no. 93, doi: [10.3390/wevj13050093](https://doi.org/10.3390/wevj13050093).
- [46] M. Ehsani, Y. Gao, S. Longo, and K. Ebrahimi, *Modern Electric, Hybrid Electric, and Fuel Cell Vehicles*. Boca Raton, FL, USA: CRC Press, 2018.
- [47] F. Papini and M. Osama, "Electromagnetic design of an interior permanent magnet motor for vehicle traction," in *Proc. XIII Int. Conf. Elect. Mach.*, Alexandroupoli, Greece, Sep. 3–6, 2018, pp. 205–211, doi: [10.1109/ICELMACH.2018.8507222](https://doi.org/10.1109/ICELMACH.2018.8507222).
- [48] S. Mirzaei and A. Fernandez, "Retard system solution on electric mining trucks," in *Proc. IEEE 3rd Int. Symp. Sensorless Control Elect. Drives*, Milwaukee, WI, USA, 2012, pp. 1–5, doi: [10.1109/SLED.2012.6422816](https://doi.org/10.1109/SLED.2012.6422816).
- [49] G. Pellegrino, A. Vagati, B. Boazzo, and P. Guglielmi, "Comparison of induction and PM synchronous motor drives for EV application including design examples," *IEEE Trans. Ind. Appl.*, vol. 4, no. 6, pp. 2322–2332, Nov./Dec. 2012, doi: [10.1109/TIA.2012.2227092](https://doi.org/10.1109/TIA.2012.2227092).
- [50] K. Aiso and K. Akatsu, "Performance comparison of high-speed motors for electric vehicle," *World Electric Veh. J.*, vol. 13, 2022, Art. no. 57, doi: [10.3390/wevj13040057](https://doi.org/10.3390/wevj13040057).
- [51] V. Dmitrievskii, V. Prakht, E. Valeev, A. Paramonov, V. Kazakbaev, and A. Anuchin, "Comparative study of induction and wound rotor synchronous motors for the traction drive of a mining dump truck operating in wide constant power speed range," *IEEE Access*, vol. 11, pp. 68395–68409, 2023, doi: [10.1109/ACCESS.2023.3292244](https://doi.org/10.1109/ACCESS.2023.3292244).
- [52] A. G. Sarigiannidis, M. E. Beniakar, and A. G. Kladas, "Fast adaptive evolutionary PM traction motor optimization based on electric vehicle drive cycle," *IEEE Trans. Veh. Technol.*, vol. 66, no. 7, pp. 5762–5774, Jul. 2017, doi: [10.1109/TVT.2016.2631161](https://doi.org/10.1109/TVT.2016.2631161).
- [53] D. Zarko, S. Stipetic, M. Martinovic, M. Kovacic, T. Jeric, and Z. Hanic, "Reduction of computational efforts in finite element-based permanent magnet traction motor optimization," *IEEE Trans. Ind. Electron.*, vol. 65, no. 2, pp. 1799–1807, Feb. 2018, doi: [10.1109/TIE.2017.2736485](https://doi.org/10.1109/TIE.2017.2736485).
- [54] F. Cupertino, G. Pellegrino, and C. Gerada, "Design of synchronous reluctance motors with multiobjective optimization algorithms," *IEEE Trans. Ind. Appl.*, vol. 50, no. 6, pp. 3617–3627, Nov./Dec. 2014, doi: [10.1109/TIA.2014.2312540](https://doi.org/10.1109/TIA.2014.2312540).
- [55] K. M. Cisse, S. Hlioui, Y. Cheng, M. Belhadi, and M. Gabsi, "Optimization of V-shaped synchronous motor for automotive application," in *Proc. XIII Int. Conf. Elect. Mach.*, Alexandroupoli, Greece, 2018, pp. 906–912, doi: [10.1109/ICELMACH.2018.8507033](https://doi.org/10.1109/ICELMACH.2018.8507033).
- [56] M. Ruba et al., "Synchronous reluctance machine geometry optimisation through a genetic algorithm based technique," *IET Elect. Power Appl.*, vol. 12, no. 3, pp. 431–438, 2018, doi: [10.1049/iet-epa.2017.0455](https://doi.org/10.1049/iet-epa.2017.0455).
- [57] A. Anuchin, D. Aliamkin, M. Lashkevich, D. Shpak, A. Zharkov, and F. Briz, "Minimization and redistribution of switching losses using predictive PWM strategy in a voltage source inverter," in *Proc. IEEE 25th Int. Workshop Electric Drives: Optim. Control Electric Drives*, Moscow, Russia, Jan.-Feb. 2018, pp. 1–6, doi: [10.1109/IWED.2018.8321375](https://doi.org/10.1109/IWED.2018.8321375).
- [58] A. Yoshida and K. Akatsu, "Study of winding structure to reduce harmonic currents in dual three-phase motor," *World Electric Veh. J.*, vol. 14, 2023, Art. no. 100, doi: [10.3390/wevj14040100](https://doi.org/10.3390/wevj14040100).
- [59] M. Merdžan, "Performance analysis of high-speed electric machines supplied by PWM inverters based on the harmonic modeling method," *Energies*, vol. 14, 2021, Art. no. 2606, doi: [10.3390/en14092606](https://doi.org/10.3390/en14092606).
- [60] C. Ye, J. Yang, F. Xiong, and Z. Q. Zhu, "Relationship between homopolar inductor machine and wound-field synchronous machine," *IEEE Trans. Ind. Electron.*, vol. 67, no. 2, pp. 919–930, Feb. 2020, doi: [10.1109/TIE.2019.2898577](https://doi.org/10.1109/TIE.2019.2898577).
- [61] L. Vido, M. Gabsi, M. Lecrivain, Y. Amara, and F. Chabot, "Homopolar and bipolar hybrid excitation synchronous machines," in *Proc. IEEE Int. Conf. Electric Mach. Drives*, San Antonio, TX, USA, 2005, pp. 1212–1218, doi: [10.1109/IEMDC.2005.195876](https://doi.org/10.1109/IEMDC.2005.195876).
- [62] N. Bianchi, *Electrical Machine Analysis Using Finite Elements*. Boca Raton, FL, USA: CRC press, 2005, doi: [10.1201/9781315219295](https://doi.org/10.1201/9781315219295).
- [63] M. Zaheer, "Evaluation of open-source FEM software performance in analysing converter-fed induction machine losses," D.Sc. dissertation, Lappeenranta–Lahti Univ. Technol., Lappeenranta, Finland, 2022. [Online]. Available: <https://lutpub.lut.fi/handle/10024/163651>
- [64] A. Selema, M. Gulec, M. N. Ibrahim, R. Sprangers, and P. Sergeant, "Selection of magnet wire topologies with reduced AC losses for the windings of electric drivetrains," *IEEE Access*, vol. 10, pp. 121531–121546, 2022, doi: [10.1109/ACCESS.2022.3222773](https://doi.org/10.1109/ACCESS.2022.3222773).
- [65] S. Guo et al., "A design technique of traction motor for efficiency improvement based on multiobjective optimization," *World Electr. Veh. J.*, vol. 12, 2021, Art. no. 260, doi: [10.3390/wevj12040260](https://doi.org/10.3390/wevj12040260).
- [66] Y. Sun, Y. Fang, Q. Zhang, and Q. Liu, "Optimal design of marine motors for joint efficiency and economic optimization," *Energies*, vol. 16, 2023, Art. no. 4588, doi: [10.3390/en16124588](https://doi.org/10.3390/en16124588).
- [67] J. Goss, M. Popescu, and D. Staton, "A comparison of an interior permanent magnet and copper rotor induction motor in a hybrid electric vehicle application," in *Proc. IEEE 2013 Int. Electric Machines Drives Conf.*, Chicago, IL, USA, May 12–15, 2013, pp. 220–225, doi: [10.1109/IEMDC.2013.6556256](https://doi.org/10.1109/IEMDC.2013.6556256).
- [68] B. Cougo, L. M. F. Morais, G. Segond, R. Riva, and H. Tran Duc, "Influence of PWM methods on semiconductor losses and thermal cycling of 15-kVA three-phase SiC inverter for aircraft applications," *Electronics*, vol. 9, 2020, Art. no. 620, doi: [10.3390/electronics9040620](https://doi.org/10.3390/electronics9040620).



[69] "Infineon online power simulation platform," Accessed: Sep. 18, 2023. [Online]. Available: [https://www.infineon.com/cms/en/tools/landing/ iposim-infineon-online-power-simulation-platform](https://www.infineon.com/cms/en/tools/landing/iposim-infineon-online-power-simulation-platform)

[70] IGBT Modules, "Infineon online catalogue," Accessed: Sep. 18, 2023. [Online]. Available: <https://www.infineon.com/cms/en/product/power/igbt/igbt-modules>



**VLADIMIR PRAKHT** received the Graduate degree in engineering and the Ph.D. degree from the Department of Electrical Engineering, Ural Federal University, Yekaterinburg, Russia, in 2004 and 2007, respectively. He submitted his Ph.D. dissertation on optimal control and mathematical modeling induction heating systems in 2006. He is currently an Associate Professor with the Department of Electrical Engineering, Ural Federal University. His research interests include mathematical modeling and optimal design of energy

efficient electric motors and generators.



**VLADIMIR DMITRIEVSKII** received the master's degree in theoretical physics and the Ph.D. degree from Ural Federal University, Yekaterinburg, Russia, in 1996 and 2007, respectively. He submitted his Ph.D. dissertation on mathematical modeling and optimal designing linear electric motors in 2006. He is currently an Associate Professor with the Department of Electrical Engineering, Ural Federal University. His research interests include optimal designing energy-efficient motors and developing sensorless control algorithms for electric drives.



**VADIM KAZAKBAEV** received the Graduate degree in engineering and the Ph.D. degree from the Department of Electrical Machines, Ural Federal University, Yekaterinburg, Russia, in 2010 and 2017, respectively. He submitted his Ph.D. dissertation on "Development of High-Performance Synchronous Reluctance Motor" in 2016. He is currently a Junior Researcher and also an Associate Professor with the Department of Electrical Engineering, Ural Federal University. His research interests include electrical engineering, design of

electrical machines, and control of electrical drives.



**EDUARD VALEEV** is currently working toward the master's degree with the Department of Electrical Engineering, Ural Federal University, Yekaterinburg, Russia. He is also a Laboratory Assistant with the Department of Electrical Engineering, Ural Federal University. His research interests include modeling of electrical drive systems.



**ALEKSEY PARAMONOV** is currently working toward the master's degree with the Department of Electrical Engineering, Ural Federal University. He is also a Laboratory Assistant with the Department of Electrical Engineering, Ural Federal University. He has prepared and has authored or coauthored several articles on electrical system modeling in scientific peer-reviewed journals. His research interests include modeling of electrical machines and electrical drive systems.



**ALEKSEY ANUCHIN** (Senior Member, IEEE) received the B.Sc., M.Sc., Ph.D., and Dr.Eng.Sc. degrees from Moscow Power Engineering Institute, Moscow, Russia, in 1999, 2001, 2004, and 2018, respectively. He currently delivers lectures on "control systems of electric drives," "real-time software design," "electric drives," and "science research writing" with Moscow Power Engineering Institute. He was in a Head Position with the Electric Drives Department for the last eight years.

He has more than 20 years of experience covering control systems of electric drives, hybrid powertrains, and real-time communications. He has authored or coauthored more than 100 conference and journal papers. He is the author of three textbooks on the design of real-time software for the microcontroller of the C28 family and Cortex-M4F, and control system of electric drives (in Russian).